International Journal of Impact Engineering 156 (2021) 103957

Contents lists available at ScienceDirect

International Journal of Impact Engineering

journal homepage: www.elsevier.com/locate/ijimpeng

Ballistic perforation resistance of thin concrete slabs impacted by ogive-nose steel projectiles

Martin Kristoffersen [a,b], Oda L. Toreskås [c], Sumita Dey [c], Tore Børvik [a,b,c,*]

[a] Structural Impact Laboratory (SIMLab), Department of Structural Engineering, NTNU – Norwegian University of Science and Technology, Trondheim, Norway
[b] Centre for Advanced Structural Analysis (CASA), NTNU, Trondheim, Norway
[c] Research and Development Department, Norwegian Defence Estates Agency, Oslo, Norway

ARTICLE INFO

Keywords:
Concrete
Impact tests
Material tests
Numerical simulations
Ballistic limits
LS-DYNA simulations

ABSTRACT

Concrete is a material frequently used in protective structures exposed to extreme loading. In this study, the ballistic perforation resistance of 50 mm thick plain concrete slabs impacted by 20 mm diameter ogive-nose steel projectiles is investigated both experimentally and numerically. Three types of commercially produced concrete with nominal unconfined compressive strengths of 35, 75 and 110 MPa were used to cast material test specimens and slabs. After curing, ballistic impact tests were carried out in a compressed gas gun facility to determine the ballistic limit curve and velocity for each concrete type. Alongside the impact tests, material tests were conducted to assess the mechanical properties of the materials. Finite element models using input from the material tests were established in LS-DYNA. Here, the constitutive behaviour of the three concrete types was predicted by a modified version of the Holmquist-Johnson-Cook (MHJC) model from the literature. Numerical simulations of the ballistic impact tests were finally carried out and the results were found to be in good agreement with the experimental data. The main objective of the study is to reveal the accuracy of the MHJC model in predicting the ballistic perforation resistance of concrete slabs impacted by ogive-nose steel projectiles using standard material tests and two-dimensional digital image correlation to calibrate the constitutive relation.

1. Introduction

Concrete is a material frequently used for fortification installations in the process, nuclear and defence industries, where protective structure applications may not be limited by weight and space constraints [1]. Due to its widespread use in critical infrastructure, many studies on the behaviour of concrete components exposed to extreme loadings such as ballistic impact can be found in the literature. These studies generally revolve around experimental investigations, analytical models and numerical simulations, or any combination of these methods.

Until the 21st century, most ballistic impact studies on concrete were of an empirical nature. In these works, the targets were typically separated into semi-infinite targets and slabs with a finite thickness. The former minimises lateral boundary effects in order to study deep penetration into massive concrete structures [2,3], while the latter aims to study projectile perforation [4,5]. From these and similar works, a number of empirical formulae [6,7] and simplified analytical models [8,9] were established. For slabs with a finite thickness the penetration and perforation process is complex, and the findings are not conclusive. According to Kennedy [6], once the initial projectile velocity is large enough to penetrate the concrete, pieces of concrete spall from the impact face of the target, forming a crater that extends over an area much larger than the impact zone. As projectile velocity is increased, the projectile penetrates to depths greater than that of the spall crater, producing a hole (tunnel) into the concrete with a diameter only slightly larger than the projectile diameter. A further increase in the projectile velocity results in cracking and then scabbing of concrete from the rear surface. The scabbing zone area is generally more expansive, but less deep, than that of the front spall crater. Once scabbing begins, the thickness of the target is reduced, and the depth of penetration increases rapidly with increasing projectile velocity, leading eventually to perforation of the slab. The various damage mechanisms involved in these processes, namely compaction, compression with moderate to high lateral pressure and tensile cracking, were later discussed by Polanco-Loria et al. [10], among others.

Hanchak et al. [4] studied the perforation resistance of 178 mm thick

* Corresponding author at: Structural Impact Laboratory (SIMLab), Department of Structural Engineering, NTNU – Norwegian University of Science and Technology, Trondheim, Norway.
E-mail address: tore.borvik@ntnu.no (T. Børvik).

https://doi.org/10.1016/j.ijimpeng.2021.103957
Received 5 January 2021; Received in revised form 28 May 2021; Accepted 30 June 2021
Available online 5 July 2021

reinforced concrete slabs with unconfined compressive strengths of 48 and 140 MPa impacted by ogive-nose steel projectiles. A strong disproportionality between compressive strength and perforation resistance was found, and a threefold increase in the compressive strength resulted in a less than 20 % increase in the ballistic limit. Hanchak et al. [4] also reported that the ballistic limit velocity was insensitive to whether the projectile struck the rebars during perforation. Similar conclusions were later drawn by Børvik et al. [11] based on impact tests using conical-nose projectiles on 100 mm thick concrete slabs with unconfined compressive strengths between 25 and 200 MPa. Here, a modest and almost linear increase in ballistic limit velocity with unconfined compressive strength was obtained (roughly 50 % when increasing the unconfined compressive strength by a factor of 8). The effects of material density and steel fibre reinforcement were found to be minimal on the perforation resistance, but no traditional rebar mesh was used in [11].

Dancygier and Yankelevsky [5] investigated the response of normal (35 MPa) and high (100 MPa) strength concrete plates with different types of reinforcement impacted by sharp projectiles. The high strength concrete showed a slightly higher perforation resistance than the normal strength concrete. However, the impact response was different since failure in the high strength concrete appeared more brittle, causing larger craters and concrete fragments to separate from the rear side, but steel fibres tended to arrest developing cracks, thus decreasing the brittleness. Conventional reinforcement using closely spaced small diameter wires was found to be less effective than fibres against penetration and spalling but showed an enhanced resistance against perforation and scabbing. Similar conclusions were later demonstrated by Dancygier [12], who also showed that higher reinforcement ratios lead to higher perforation resistance [13]. Sliter [14] also noted that reinforcement quantity has a positive effect on the perforation resistance. The same was concluded by Lee et al. [15], who in addition found that the reinforcement diameter and yield strength barely affected the impact resistance. Almansa and Cánovas [16] studied the behaviour of normal and steel fibre reinforced concrete plates with unconfined compressive strength of 45 MPa under impact of small arms projectiles. The addition of steel fibre only resulted in a small increase in perforation resistance, but the thickness needed to avoid scabbing was reduced by about 20 % compared with plain concrete. The effect of steel bar reinforcement on the penetration depth in thick concrete targets has been studied both experimentally and numerically by e.g. Zhang et al. [17], who found that reinforcement improved the penetration resistance, and even more so if the projectile hit the reinforcement directly or if the reinforcement had a shallow concrete cover.

Before the 21st century, numerical simulations of ballistic impact on concrete structures were rare, but some exceptions can be found in [18–20] for example. With the rapid development of computational tools over the last two decades, more recent studies have used numerical simulations to model the penetration and perforation process of concrete targets. These works often include experimental tests used mainly to validate the numerical models and results. Examples of recent studies on the ballistic impact of concrete slabs are available in [21–28] and in the references therein. However, most of these studies consider the behaviour of rather thick concrete targets and not thin slabs as in the present study.

Many constitutive relations for dynamic loading of concrete have also been proposed over the years. Today, the most frequently used models for extreme loading conditions on concrete structures seems to be the HJC model [18,27], the K&C model [29,30], the RHT model [31,32] and the CDP model [33,34]. These constitutive relations are implemented in various commercial non-linear finite element solvers like LS-DYNA [35] and ABAQUS [36].

Since the dynamic response of concrete structures under extreme loading is highly complex, all these models have strengths and weaknesses. The simplicity of implementation and calibration for the HJC model is advantageous, but the omission of the third invariant or the Lode angle (known to be important for concrete [37]), for example, means it is often considered too simple. The K&C, RHT and CDP models are more advanced, but they require many model constants calibrated from material tests not necessarily available in design. This has been partly overcome by implementing an automatic parameter generator in some solvers where model constants are determined solely based on the cylinder compressive strength of the material. Even though this significantly simplifies the calibration, the accuracy of the automatically generated constants is uncertain [38] and the calibration process itself becomes a black box for the users.

Polanco-Loria et al. [10] proposed some modifications to the original HJC model. Firstly, the influence of the third deviatoric stress invariant was included to enhance the pressure-shear behaviour; this accounts for the substantial shear strength difference between the tensile and compressive meridians of concrete. Secondly, the strain-rate sensitivity model was changed so that the strain-rate enhancement factor goes to unity for zero strain rate. Thirdly, different damage variables to describe tensile cracking, shear cracking and pore compaction mechanisms were introduced. These modifications to the HJC model were intended as an engineering compromise between simplicity and accuracy rather than using the more demanding models. However, the modified HJC (or MHJC) model was only validated against some data from the literature in [10].

In this study, the main objective is to demonstrate the accuracy of the MHJC model in predicting the ballistic perforation resistance of concrete slabs impacted by ogive-nose steel projectiles using standard material tests and digital image correlation (DIC) to calibrate the constitutive relation. The extensive experimental database obtained based on these high-precision tests may also serve to validate other concrete models available in commercial codes. Thus, the ballistic perforation resistance of concrete slabs impacted by ogive-nosed steel projectiles is investigated both experimentally and numerically in the following. Firstly, 50 mm thick slabs from three types of commercially produced concrete with nominal unconfined compressive strengths of 35, 75 and 110 MPa were cast. In addition to the slabs, cubes and cylinders for material tests were made from the same concrete batches. After curing, ballistic impact tests were carried out in a compressed gas gun facility using 20 mm diameter, 196 gram mass, ogive-nose hard steel projectiles to determine the perforation resistance of the various concrete slabs. Synchronised high-speed cameras were used to measure the initial and residual velocity of the projectiles during testing, and the ballistic limit velocity of each concrete slab type was determined. Parallel to the impact tests, quasi-static material tests (cube compression, cylinder compression and tensile splitting) were conducted to assess the mechanical properties of the materials. In these tests, the force measurements from the load cell were synchronised with local displacement-field measurements using DIC to capture the stress-strain behaviour of the materials. Finite element models using input from the material tests were then established in LS-DYNA. Here, the constitutive behaviour of the different concretes was predicted by the MHJC model. Numerical simulations of the ballistic impact tests were run, and good agreement between the experimental and numerical results were obtained. Both the experiments and the simulations suggest that the tensile strength is the most dominant material parameter governing the behaviour of the thin concrete slabs used in this study during ballistic impact.

2. Concrete types

Three different concrete mixtures were used for the slabs in this study, and the mixture proportions are given in Table 1. The mixtures were composed such that the nominal unconfined compressive strengths should be above 35 MPa (C35), 75 MPa (C75) and 110 MPa (C110). All three concrete types were produced by a commercial supplier and delivered by a mixer truck to the concrete laboratory at NTNU. Upon delivery, the air content, slump, and density of the fresh concrete were measured (see Table 1). The slump was found to be in the range of 200

Table 1
Mixture proportions and fresh concrete properties for the different concrete types.

Concrete type	C35	C75	C110
Cement (kg/m^3)	305	427	536
Silica fume (kg/m^3)	13	48	103
Water (kg/m^3)	181	168	140
Fine aggregate: 0-8 mm (kg/m^3)	1079	917	857
Coarse aggregate: 8-16 mm (kg/m^3)	845	881	835
MasterGlenium SKY 899 (kg/m^3)	1.5	4.1	10.7
W/C-ratio	0.59	0.39	0.26
Air content (%)	1.0	1.2	1.1
Slump (mm)	205	200	230
Density of fresh concrete (kg/m^3)	2501	2491	2550

mm and the workability was found to be satisfactory for all three concrete types.

Concrete slabs with nominal dimensions 625 mm × 625 mm × 50 mm were cast in custom-made wooden moulds. A total number of 12 slabs were cast for each concrete type. Smooth lubricated plastic tubes were inserted through 12 equally spaced cut-outs for bolt holes in the moulds before the concrete was poured. A reinforcement bar with diameter 8 mm looping on the outside of the bolt holes was added to provide a lifting point and to prevent the slabs from falling apart after the ballistic tests in case of extensive damage. Thus, the central part of the slabs to be impacted by projectiles were plain concrete in this study, and the effect of reinforcements (either by rebars or steel fibres) on the perforation resistance of the concrete slabs is not considered. An investigation of this concern, however, is recommended for further studies since the published literature on this issue is somewhat inconsistent (see e.g. [4,13] [15,39]). The slabs were demoulded the day after casting, wrapped in wet burlap, covered with plastic sheets and stored at room temperature to provide good curing conditions until the day of testing. The wooden moulds used to cast the concrete slabs and a typical slab with dimensions are shown in Fig. 1. In addition to the concrete slabs, cubes and cylinders were cast in reusable steel moulds for material testing. The material test specimens were also demoulded the day after casting but were kept submerged in water at room temperature until the day of testing.

3. Material tests

Cylinder compression, cube compression and tensile splitting (Brazilian) tests were performed on all three concrete types. The cylinders were 100 mm in diameter and 200 mm long, while the cubes had side lengths of 100 mm. All tests were carried out in a fully automated Toni Tech 3000 kN load controlled rig at a loading rate of 0.8 MPa/s. Table 2 gives the mass density ρ_0, the cylinder compressive strength f_c, the cube compressive strength f_{cc}, the tensile splitting strength f_t, and the Poisson ratio ν of the concrete types 28 days after casting. In addition, separate cube compression tests were carried out at different numbers of days D_t to monitor the strength development of each concrete type. The results are plotted in Fig. 2, along with a least squares fit to the following equation

$$f_{cc}(D_t) = \bar{f} \cdot \exp\left(s \cdot \left[1 - \frac{\bar{D}}{D_t}\right]\right) \tag{1}$$

where $\bar{f}$, s and $\bar{D}$ are constants determined for each concrete type, given in Table 2.

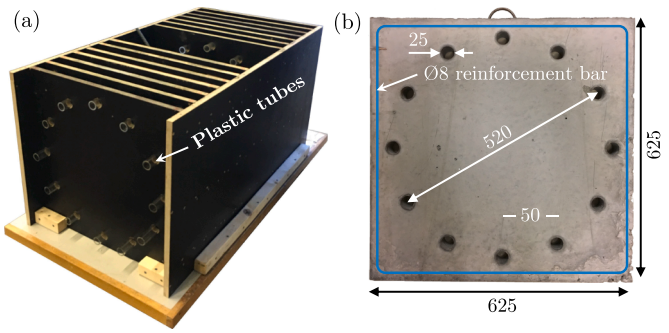

Fig. 1. (a) Wooden moulds used to cast slabs and (b) concrete slab with dimensions (in mm).

Some of the material tests were instrumented with DIC (using the in-house 2D/3D DIC code eCorr [40]) to provide data for calibration of the MHJC model [10]. The specimens were painted with a speckled pattern as exemplified by the top row of images in Fig. 3. The images were synchronised with the force measurements, which are plotted to the right in Fig. 3 with a circle marker identifying each image included. In the analysis, the distance ℓ between 11 opposing subset pairs – shown as yellow squares at the bottom row of Fig. 3 – gave 11 estimates of the engineering strain e_{ax} in the load direction through the relation $e_{ax} = (\ell - \ell_0)/\ell_0$, where ℓ_0 is the initial distance. As supported by the effective strain field on image 595 in Fig. 3, the estimated strains from the subset motions were close to homogeneous up to the appearance of the first cracks (image 602). The data started deviating notably after the peak load (image 603). Therefore, to represent each test, the average value of the 11 strain measurements up to the peak load was used, and the values based on image 603 are excluded from the strain curve plotted in Fig. 3. This plot shows the average value of the 11 strain measurements together with the synchronised force measurement for each of the 603 images from the test. The average curve of three separate tests was used to represent the material for each test type.

Separate subset analyses were run for the cubes to estimate the Poisson ratio ν. To this end, five subset pairs were used to measure the strain in the loading direction e_{ax} like before. Five additional subset pairs were set up to measure the strain the in the transverse direction $e_{tr} = (b - b_0)/b_0$ as illustrated in Fig. 4(a), where b is the current horizontal distance between the subset pairs, and b_0 is the corresponding initial distance. The Poisson ratio is then obtained as

$$\nu = -\frac{e_{tr}}{e_{ax}} \tag{2}$$

In the initial phase of the test, i.e., when the rig makes firm contact with the specimen and the force starts increasing, the strains are very small and the value for the Poisson ratio varies a lot from one image to the next. After the force increases and the specimen settles, the Poisson ratio stabilises. When the test approaches the peak load and the concrete starts cracking, the Poisson ratio once again varies notably. Thus, a section of the test within the linear elastic domain was chosen to determine ν, illustrated by the vertical dotted lines in Fig. 4(b). These limits were chosen manually on a test-by-test basis. The average value of ν within those limits determined the Poisson ratio, and the values are given in Table 2 (mean value of three tests).

Although the curved surface was the only visible part of the specimen in the cylinder compression tests, the same procedure as for the cube specimens, using only one camera during testing, was employed because the out-of-plane deformations were negligible up to first fracture. The scatter between the tests within the same series was low for the cube compression and cylinder compression tests, but notably higher for the tensile splitting tests. This result comes from the strain levels being one order of magnitude lower for the tensile splitting tests, which makes the noise in the measurements more pronounced.

All DIC instrumented material tests were performed 28 days after casting for the C75 and C110 concretes as intended. For the C35 concrete, however, the DIC instrumented cube compression and tensile splitting tests were performed 34 days after casting, while the cylinder compression tests with DIC were performed 41 days after casting due to delays in vital equipment delivery. It was for this reason that the strength development of the concrete over time was carefully tracked, as

Table 2
Least squares fits of the strength development constants in Eq. (1) and material test results 28 days after casting (average of three tests).

Concrete type	Least squares fits for Eq. (1)				Material test results			
	$\bar{f}$	s	$\bar{D}$	ρ_0	f_c	f_{cc}	f_t	ν
	[MPa]	[-]	[days]	[kg/m^3]	[MPa]	[MPa]	[MPa]	[-]
C35	52.6	0.465	31.3	2467	44.6	47.6	4.0	0.25*
C75	95.0	0.352	34.4	2506	72.8	87.4	5.2	0.24
C110	128.8	0.265	28.3	2570	112.5	123.6	6.2	0.22

*Obtained from tests performed after 34 days.

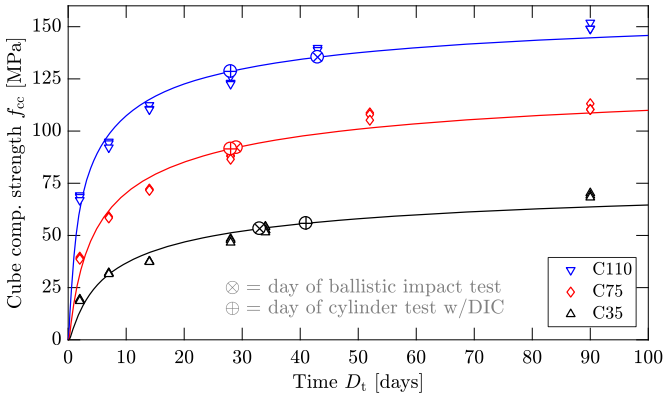

Fig. 2. Cube compressive strength of the C35, C75 and C110 concrete types as a function of days after casting D_t, where the solid lines are based on a least squares fit to Eq. (1).

displayed in Fig. 2. The complications encountered because of the delay highlight the inevitable challenges associated with the testing and modelling of concrete. For all three concrete types, the material tests are deemed sufficiently close in time to the ballistic tests to be representative of the general material behaviour.

The engineering stress-strain curves resulting from the cylinder compression tests, the cube compression tests and the tensile splitting tests of all three concrete types are given in Fig. 5. The curves are plotted until peak load, after which the strain fields became increasingly inhomogeneous and the DIC code lost correlation due to cracking as indicated in Fig. 3. The results were generally in accordance with expectations, except for the tensile splitting tests where the C35 concrete appeared stiffer than the C75 concrete. The peak loads for the tensile splitting tests were consistent with the compression tests. However, while the cube and cylinder compression tests were quite similar both quantitatively and qualitatively for all three concrete types, there was more scatter in the tensile splitting data. It should be noted that the cylinder compressive strength of the C35 concrete was higher than the cube compressive strength because of the difference in curing time for the DIC tests. Also, the ratio f_t/f_c decreased for concrete from low-strength to high-strength, similar to previous works [4,11,41]. Note that the estimated engineering stress-strain curves are not necessarily representative for the intrinsic material properties, particularly for the tensile splitting test [42]. The cylinder compression test will be used for calibration of material constants by inverse modelling, which has been a successful approach in previous work [43].

4. Component tests

4.1. Experimental setup

The ballistic impact tests were performed in a compressed gas gun facility described in detail in Børvik et al. [44]. The main components of the gas gun are a 200 bar pressure tank, a firing unit for compressed gas, a 10 m long smooth barrel of calibre 50 mm and a closed 16 m^3 impact chamber. The gas gun is designed to launch a 250 g projectile/sabot package to a maximum velocity of 1000 m/s when helium is used as propellant [45]. In these tests, the sabot-mounted projectiles were fired at impact velocities just below and well above the ballistic limit of the concrete slabs by using compressed air. The 3D-printed serrated sabot separated immediately after leaving the barrel of the gas gun, and the sabot pieces were stopped in a sabot trap located approximately 1.5 m behind the muzzle.

The projectiles were manufactured from Arne tool steel, and heat treated to a Rockwell C value of 53 after machining. Nominal diameter (d_p = 20 mm), length (l_p = 95 mm), mass (m_p = 196 g) and critical-radius-head (CRH = 3) of the projectile were kept constant in all tests, and the geometry is shown in Fig. 6. The concrete slabs with dimensions 625 mm × 625 mm × 50 mm (see Section 2) were securely fixed to a rigid boundary in the impact camber of the gas gun by massive clamps at each corner. Even though the concrete slabs were equipped with holes for a bolted connection to the clamping system in the impact chamber, these were not used in the ballistic impact tests (but will be used in subsequent work including other experimental setups). Thus, the boundary conditions during testing were well defined although not fully

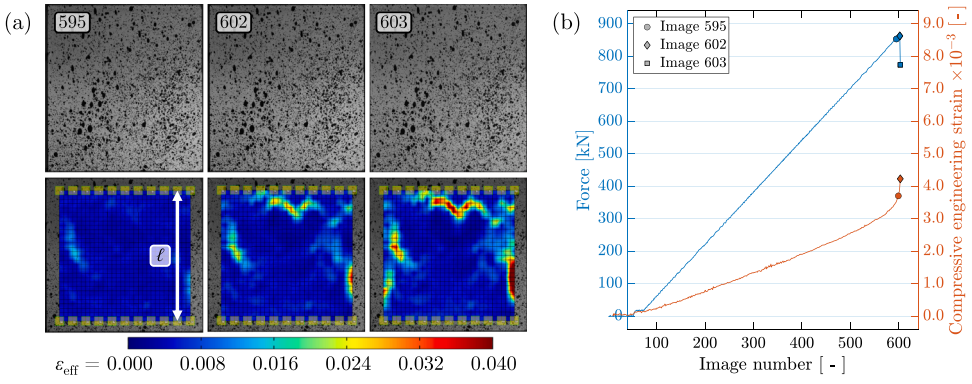

Fig. 3. (a) Effective strain field $\varepsilon_{eff} = \sqrt{\frac{4}{3}(\varepsilon_1^2 + \varepsilon_1\varepsilon_2 + \varepsilon_2^2)}$ as measured by DIC [40] on a cube compression test of the C75 concrete, where ε_1 and ε_2 are the in-plane principal logarithmic strains. The top row shows the images as recorded in the test with visible cracks highlighted in yellow, while the bottom row shows the strain field superposed on the picture. The measured force and compressive engineering strain in the load direction for each image throughout the test are plotted in (b) .

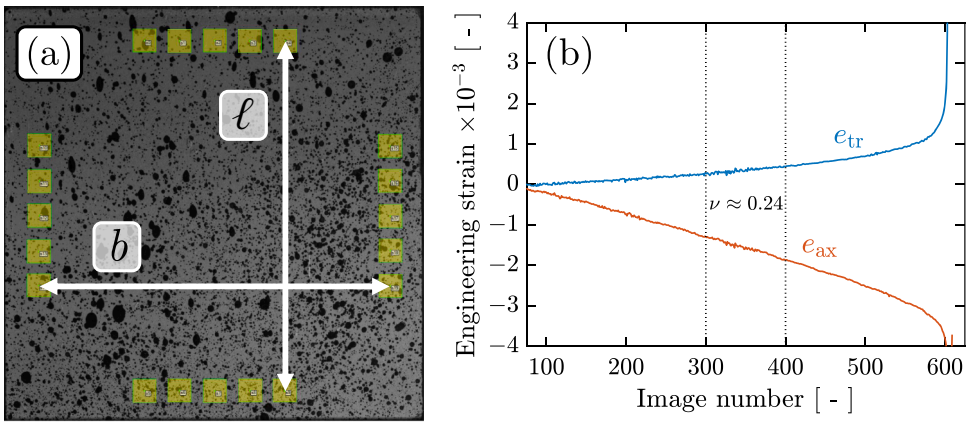

Fig. 4. Subsets used for determining Poisson ratio shown in (a), while (b) shows the resulting axial and transverse strains based on the subset tracking. The example specimen used is the same as in Fig. 3.

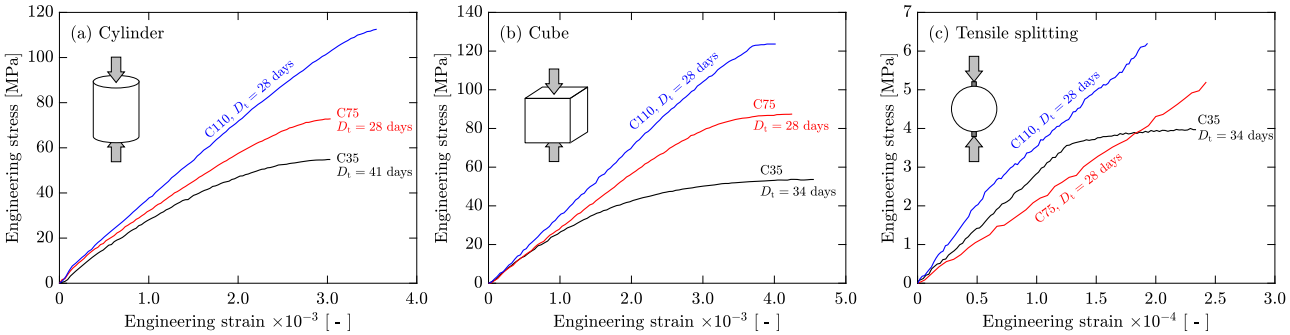

Fig. 5. Average engineering stress-strain curves from (a) cylinder compression tests, (b) cube compression tests, and (c) tensile splitting tests of all three concrete types.

clamped. It is, however, believed that the boundary conditions are of minor importance in ballistic impacts if the in-plane distance between single shots is large enough [46]. In these tests, only one shot was fired at the centre of each slab before it was replaced.

Accurate optical measurements of the initial velocity v_i and the residual velocity v_r of the projectile were provided by two Phantom v2511 high-speed cameras synchronised in time and operating at 50 000 fps, while lighting was offered by two Cordin 550 J flashlights in combination with powerful halogen lamps. As long the projectile was visible, its velocity could be tracked during the perforation process. The synchronised high-speed cameras were also used to measure projectile pitch before impact, and to capture high-resolution videos of the penetration and perforation process. In the tests, one camera and one flashlight were focused on the front side of the concrete slab to capture penetration and spalling, while the other camera and flashlight were focused on the back side of the concrete slab to capture perforation and scabbing. This was necessary to obtain good measurements due to the large number of fragments and dust ejected from the brittle targets during impact. In addition, all projectiles and concrete slabs were weighed both before and after testing.

4.2. Experimental results

The main experimental data from the ballistic impact tests, presented in terms of initial target thickness h_t, projectile pitch β_p at impact, projectile initial velocity v_i, projectile residual velocity v_r, spall crater diameter d_{spall}, scab crater diameter d_{scab}, target initial mass m_i and target final mass m_f, are given in Table 3. The mass loss of the projectile during perforation was also registered, but it never exceeded 0.25 g, so this is not reported in detail.

From Table 3, some interesting results are revealed. The average target thickness, measured by a calliper at 12 different positions along the outer edge of each slab, was in general 2-3 % higher than the nominal value. However, for one slab (test C110-6), the measured thickness was as much as 14 % higher than the nominal value. The pitch angle (measured clockwise just before impact based on the high-speed camera images) was never above 1.5°. It is believed that such low pitch angles will not affect the ballistic limit velocity, as reported in [47]. Note that the yaw angle α_p was not measured in these tests, so that the total yaw, defined as $\gamma_p = \arctan((\tan^2\alpha_p + \tan^2\beta_p)^{1/2})$, is not known. The spall and scab crater diameters were roughly measured by a ruler in the horizontal (first number in Table 3) and vertical (second number in Table 3) directions. As seen, the scab crater diameter was in general significantly larger than the spall crater diameter, which is in line with observations in previous studies [6,48]. Fig. 7 shows pictures of the irregular spall and scab craters from typical tests. It should also be noted that both the spall and scab crater diameters seem to increase with concrete strength, while there is no observable effect of impact velocity on the crater diameters. The former is confirmed by the mass loss of the concrete slabs during perforation and was also observed by Dancygier and Yankelevsky [5]. While the average mass loss for the C35 slabs was less than 0.5 kg, the average mass loss was 0.6 kg and 1.0 kg for the C75 and C110 slabs, respectively. The largest mass loss was found for the thickest slab, i.e., test C110-6, where 1.6 kg mass was lost during perforation. Omitting the C110-6 test as an outlier brings the average mass loss for the C110 concrete down to 0.9 kg, which is still notably higher than for the other two concrete types.

One slab of each concrete type was sliced through the penetration channel to show the profiles of the craters. Opposing sliced surfaces for these slabs are shown in Fig. 8, where the spalling volume is confirmed

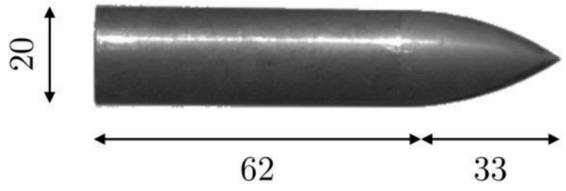

Fig. 6. Dimensions in mm of the ogive-nose steel projectile.

to be smaller than the scabbing volume. In concrete perforation experiments there is typically a tunnelling section connecting the spalling and scabbing craters [4], but in this case using thin slabs the craters are connected without any clear tunnelling section between them.

Fig. 9 shows time lapses of the penetration and perforation process based on the high-speed camera images from typical impact tests of the different concrete types. All tests are at impact velocities close to their respective ballistic limits. One camera was focused on the front side and the other camera was focused on the back side of the concrete slabs, so that both spalling and scabbing could be studied. Keep in mind that since the cameras were synchronised, they have the same timeline. As seen, a large amount of debris was ejected from the concrete slabs during impact, and it was occasionally hard to identify the projectile before it had travelled a certain distance from the slab after perforation (exemplified by the bottom row in Fig. 9). The projectiles are marked with an arrow in the last image for each concrete type. Note that the images have been cropped for brevity. Thus, it was still possible to point track the end and/or the tip of the projectile to determine the residual velocities in most cases. Otherwise, the experimental test was omitted from the test programme.

Tracking the projectile's motion during the penetration process provided data to plot its velocity as a function of time in Fig. 10. All curves are aligned so that $t = 0$ ms corresponds to the last high-speed image before impact. It is observed that the velocity is gradually reduced as the tip starts to penetrate, after which a period of approximately constant deceleration is entered. When the projectile emerges through a free surface and the resistance from the concrete decreases, the velocity curve starts to flatten, and a constant velocity is attained once the projectile assumes free flight again. The curves in Fig. 10 are dashed when the projectile is obscured by concrete debris. A straight dashed line is drawn from the last point in time where the projectile is visible on the front side to the first point in time where it is visible on the back side with the measured residual velocity. When the residual velocity is zero, for instance for slab C35-2 in Fig. 10(a), the curve is extended linearly by its tangent. There are fewer images for the higher velocities because the recording rate was the same for all tests, thereby making the measurement noise more pronounced.

Based on the measured initial and residual projectile velocities as given in Table 3, ballistic limit curves and velocities were estimated. This was done by least squares fits of the model constants in the generalised Recht-Ipson model [49] to the measured data. The model is defined as

$$v_r = a(v_i^p - v_{bl}^p)^{1/p} \tag{3}$$

where v_i and v_r are the measured initial and residual velocities of the projectile, respectively, while v_{bl} is the ballistic limit velocity. From conservation of momentum and energy it can be shown that $a = m_p/(m_p + m_{pl})$ and $p = 2$, where m_p is the mass of the projectile and m_{pl} is the total mass of possible plugs or fragments. In this study, however, a and p will be considered empirical constants. Fig. 11(a), (b) and (c) show plots of the measured initial versus residual velocity data for the C35, C75 and C110 concrete slabs, respectively, together with ballistic limit curves based on best fits to the Recht-Ipson model. Due to a limited number of tests and some scatter in the experimental data at impact velocities close to the ballistic limit – especially for the C110 concrete – it was hard to determine the ballistic limit velocities exactly. Therefore, the ballistic limit was taken as the highest impact velocity for which perforation was not completed and only scabbing occurred, while a and p were fitted to the experimental data. Obtained Recht-Ipson constants are given in Table 4, showing that a approached unity while p became less than 2. As seen from Fig. 11, the agreement between the experimental data and the ballistic limit curves based on the Recht-Ipson model was very good. Finally, Fig. 11(d) shows a plot of the ballistic limit velocity versus cube compressive strength f_{cc}. A modest and rather linear increase in ballistic limit velocity with compressive strength was obtained, which is in line with previous observations [4,11]. Here, a tripling of the unconfined compressive strength increased the ballistic limit velocity by approximately 27 %. One possible reason for this result is that a tripling of f_{cc} only increases the tensile strength f_t by 55 % (see Table 2).

5. Numerical simulations

5.1. MHJC concrete model

All numerical simulations presented in this study were run using a modified version of the Holmquist-Johnson-Cook (MHJC) model to describe the constitutive behaviour of the various concrete types. In the following, some of the main features of the MHJC model will be briefly outlined, while a full description of the model can be found in Polanco-Loria et al. [10].

The components σ_{ij} of the Cauchy stress tensor $\boldsymbol{\sigma}$ are decomposed into deviatoric and hydrostatic parts, i.e.,

$$\sigma_{ij} = \sigma'_{ij} - P\delta_{ij} \tag{4}$$

where σ'_{ij} is the stress deviator, $P = -\sigma_{kk}/3 = -(\sigma_{11} + \sigma_{22} + \sigma_{33})/3$ is the hydrostatic pressure and δ_{ij} is the Kronecker delta. The equivalent von Mises stress σ_{eq} is given as

$$\sigma_{eq} = \sqrt{\frac{3}{2}\sigma'_{ij}\sigma'_{ij}} \tag{5}$$

The components D_{ij} of the rate-of-deformation tensor $\mathbf{D}$ are defined by

$$D_{ij} = D'_{ij} + \frac{1}{3}D_{kk}\delta_{ij} \tag{6}$$

where $D_{kk} = D_{11} + D_{22} + D_{33}$. Further, D'_{ij} is the deviatoric part and is additively decomposed into an elastic part and a plastic part according to

$$D'_{ij} = D'^{e}_{ij} + D'^{p}_{ij}, D'^{e}_{ij} = \frac{\sigma^{\nabla J}_{ij}}{2G}, \; D'^{p}_{ij} = \frac{3\sigma'_{ij}}{2\sigma_{eq}}\dot{\varepsilon}^{p}_{eq} \tag{7}$$

Here, $\sigma^{\nabla J}_{ij}$ is the Jaumann rate of the stress deviator, G is the shear modulus and $\dot{\varepsilon}^{p}_{eq}$ is the equivalent plastic strain rate given as

$$\dot{\varepsilon}^{p}_{eq} = \sqrt{\frac{2}{3}D'^{p}_{ij}D'^{p}_{ij}} \tag{8}$$

The deviatoric response is determined by

$$\sigma^{*}_{eq} = \begin{cases} B[P^* + T^*(1-D)]^N F\left(\dot{\varepsilon}^{*}_{eq}\right)R(\theta,e) \le S_{max}, & P^* \ge -T^*(1-D) \\ 0, \; P^* < -T^*(1-D) \end{cases} \tag{9}$$

where $\sigma^{*}_{eq} = \sigma_{eq}/f_c$, $P^* = P/f_c$ and $T^* = T/f_c$ are the normalised equivalent stress, pressure and hydrostatic tension, respectively. T is the maximum hydrostatic tension the material can withstand and assumed equal to f_t [10]. Further, B is the pressure hardening coefficient, N is the pressure hardening exponent and S_{max} is the normalised maximum strength achievable. The strain-rate sensitivity is described by the

Table 3
Results from ballistic impact tests.

Concrete Type	Slab #	h_t [mm]	β_p [°]	v_i [m/s]	v_r [m/s]	d_{spall} [mm]	d_{scab} [mm]	m_i [kg]	m_f [kg]
C35	2	51.8	0.0	119.7	0.0	70/60	170/140	47.2	46.8
	5	50.8	1.0	137.7	44.8	80/60	120/120	49.1	48.7
	9	52.1	0.5	155.3	55.3	70/70	140/130	48.1	47.6
	11	50.4	0.5	185.0	104.2	80/70	150/130	47.3	46.9
	12	50.6	1.5	206.4	122.1	90/90	160/130	47.9	47.4
	8	51.1	1.5	245.0	173.1	90/100	130/130	47.5	47.2
	6	50.6	1.5	294.3	219.3	100/110	150/120	49.4	48.7
C75	5	51.6	1.0	117.5	0.0	70/80	160/160	49.0	48.4
	9	51.7	1.5	140.4	0.0	100/100	180/160	49.1	48.6
	7	53.0	0.5	157.1	46.2	90/90	220/220	50.0	48.9
	11	51.8	1.0	170.2	68.1	100/80	150/150	48.9	48.3
	12	51.4	0.5	206.6	115.0	90/70	120/110	47.8	47.5
	8	50.6	0.5	253.4	170.3	100/90	160/180	48.3	47.5
	10	50.4	0.0	297.9	229.1	80/110	140/120	47.9	47.5
C110	7	51.7	1.0	152.6	0.0	200/220	250/220	50.6	49.8
	1	50.9	1.0	153.6	43.3	80/110	200/140	49.1	48.8
	8	50.7	0.5	155.9	27.2	80/90	210/190	50.2	49.2
	6	56.8	1.0	163.7	14.3	80/90	280/240	54.5	52.9
	5	51.3	0.5	181.9	50.9	100/100	280/180	49.5	48.4
	2	50.5	0.0	205.8	82.4	80/90	220/200	50.8	49.6
	3	51.9	1.0	252.9	151.6	90/110	180/220	50.4	49.4
	4	50.8	0.0	302.7	208.9	110/130	200/220	48.9	47.9

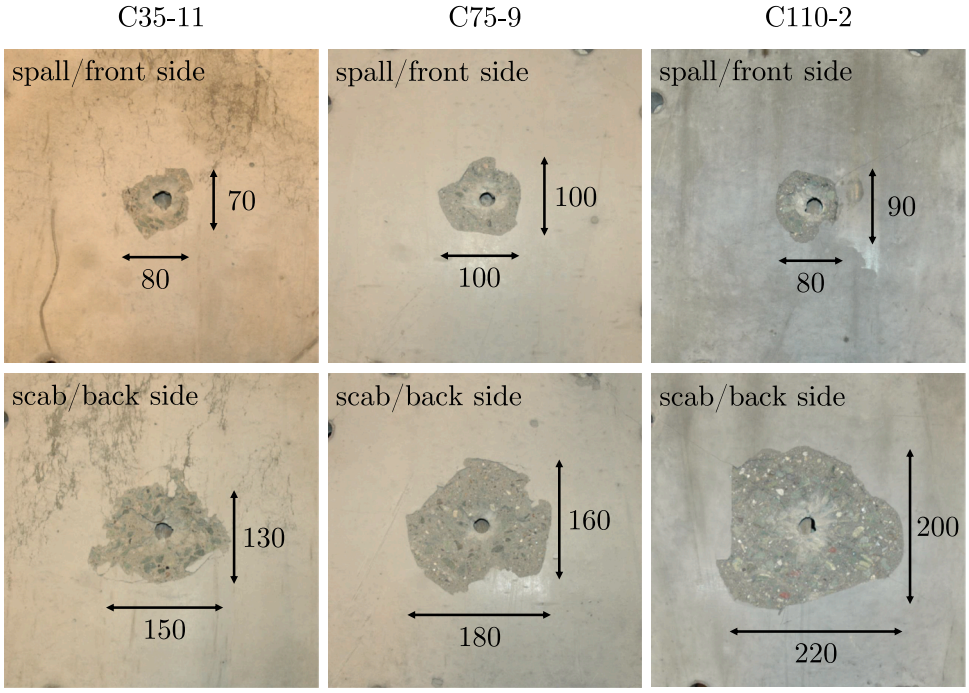

Fig. 7. Typical crater patterns after perforation, represented by test C35-11 (left column), C75-9 (centre column) and C110-2 (right column).

function

$$F\left(\dot{\varepsilon}^*_{eq}\right) = \left(1 + \dot{\varepsilon}^*_{eq}\right)^C \tag{10}$$

where $\dot{\varepsilon}^*_{eq} = \dot{\varepsilon}_{eq}/\dot{\varepsilon}_0$ is the normalised strain rate, $\dot{\varepsilon}_{eq} = \sqrt{(2/3)D'_{ij}D'_{ij}}$ is the equivalent strain rate, $\dot{\varepsilon}_0$ is a reference strain rate and C is the strain-rate sensitivity constant.

The significant difference in shear strength between triaxial compression and triaxial extension of concrete (or the influence of the third deviatoric stress invariant $J_3 = \det(\sigma'_{ij})$) is introduced by the function $R(\theta, e)$, where θ is the deviatoric (or Lode) angle and e is the normalised shape factor. The expression is given as

$$R(\theta, e) = \frac{2(1-e^2)\cos\theta + (2e-1)\left[4(1-e^2)\cos^2\theta + 5e^2 - 4e\right]^{1/2}}{4(1-e^2)\cos^2\theta + (1-2e)^2} \tag{11}$$

where the Lode angle θ is defined as

$$\theta = \frac{1}{3}\arccos\left(\frac{J_3}{\sigma^3_{eq}}\right) \tag{12}$$

Note that due to threefold symmetry, the Lode angle is confined to the interval $0 \leq \theta \leq 60^\circ$. We also note that $\theta = 0^\circ$, $\theta = 30^\circ$ and $\theta = 60^\circ$ represent generalised tension, shear, and compression, respectively. Due to convexity and smoothness of the R function, the normalised shape factor is restricted to $0.5 \leq e \leq 1$ where $e = 0.5$ forms a triangle and $e =$

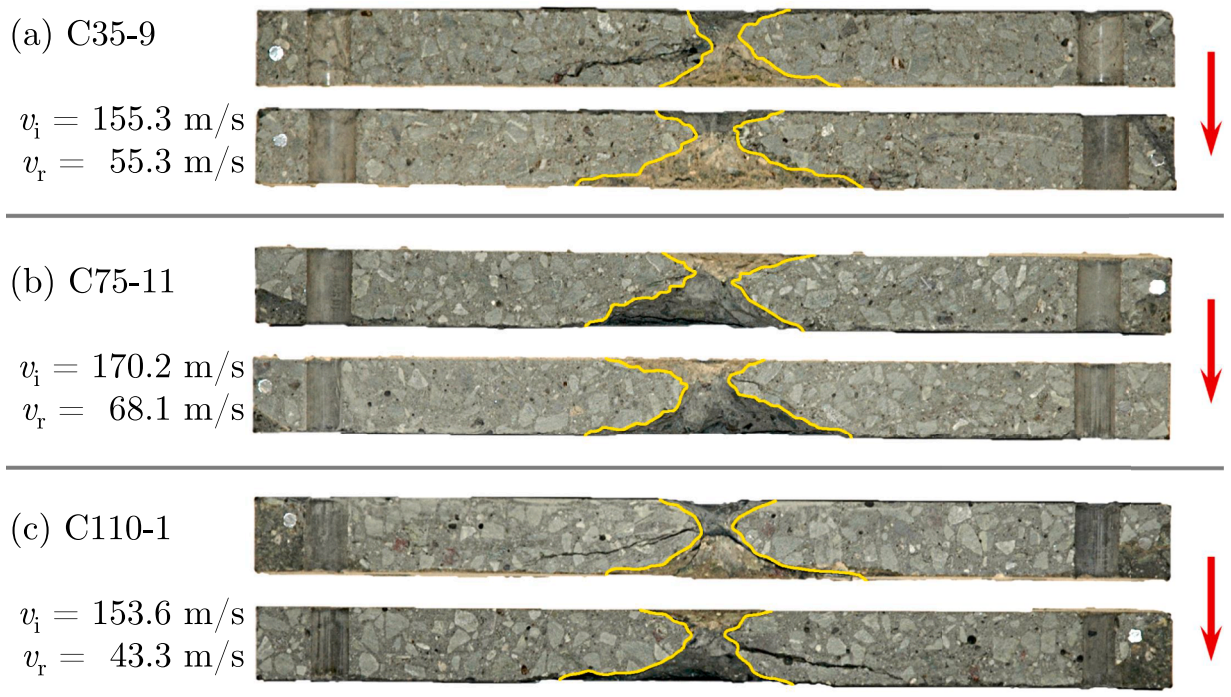

Fig. 8. Opposing cross-sectional slices of three slabs (one of each concrete type) showing the penetration channel and the spalling/scabbing craters (outlined in yellow). The arrow to the right indicates the impact direction.

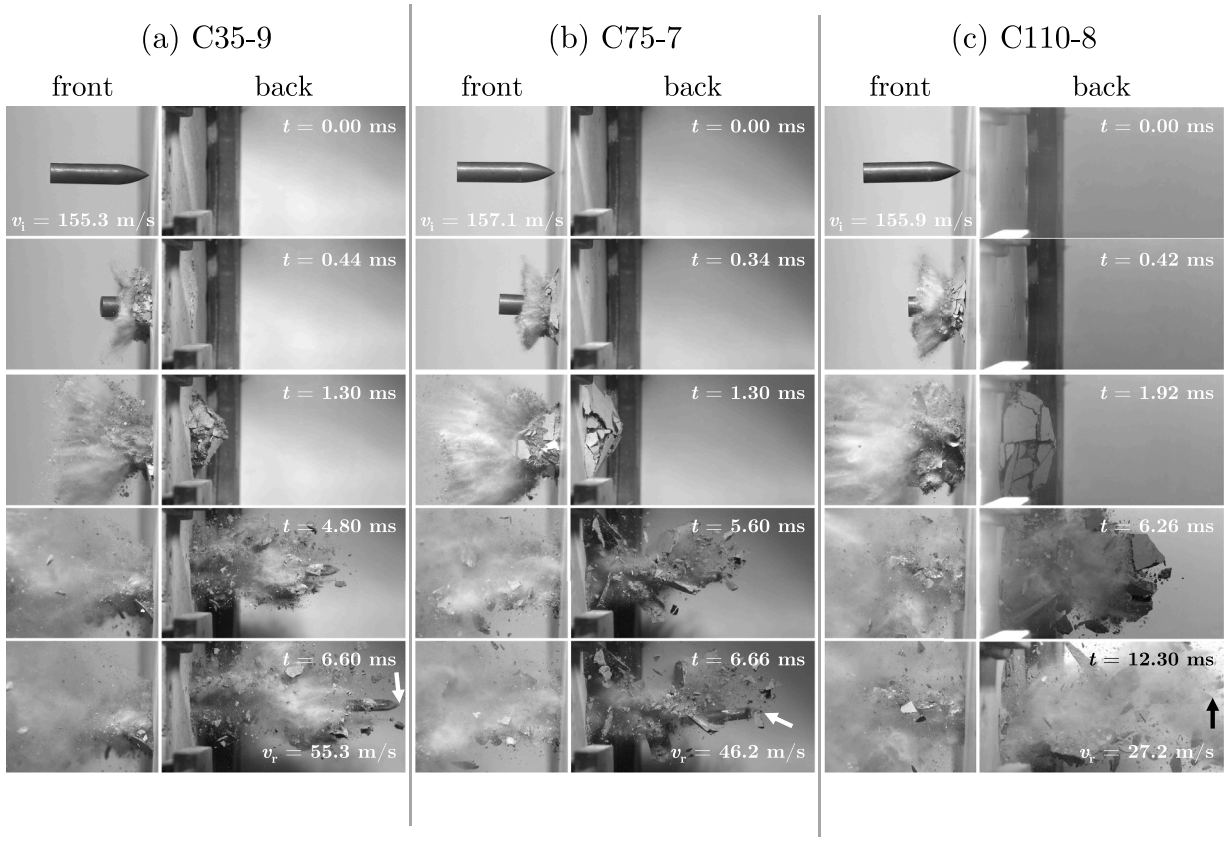

Fig. 9. Time lapse from high-speed camera images of ballistic impact tests for (a) test C35-9, (b) C75-7 and (c) C110-8 (right column). The arrows in the last row indicate the projectile after perforation.

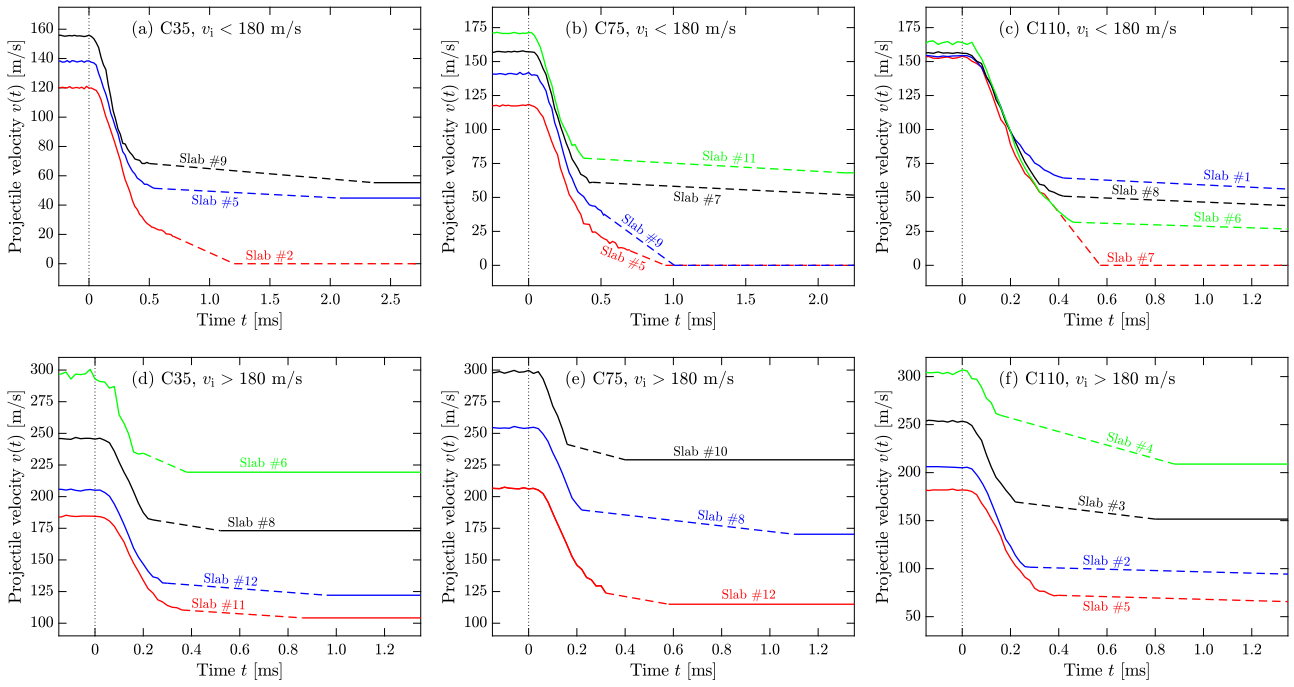

Fig. 10. Velocity-time profiles for all tests where the top row shows data for $v_i < 180$ m/s and the bottom row for $v_i > 180$ m/s. The left column is concrete type C35, the middle column C75, and the right column C110. The dashed part of the curves indicates the duration for which the projectile was obscured by concrete debris.

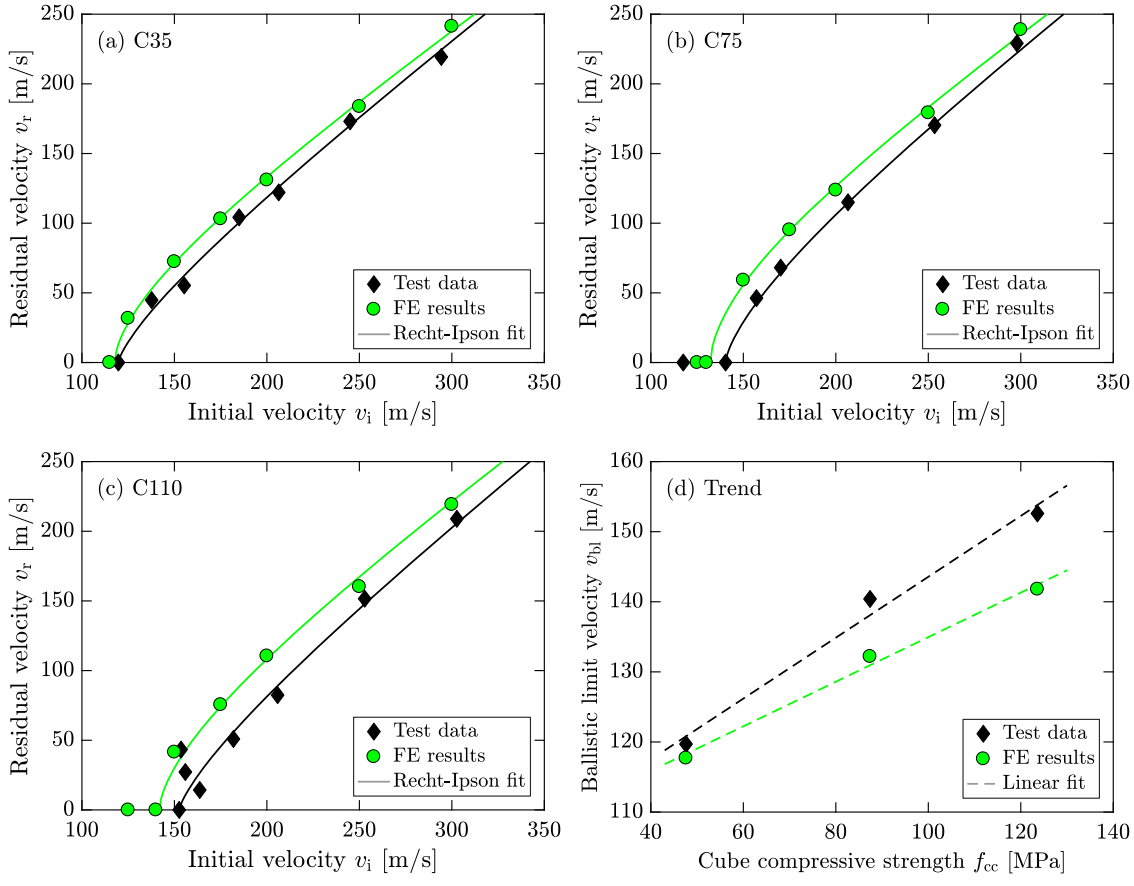

Fig. 11. Data points and ballistic limit curves based on test data and FE simulations for concrete type (a) C35, (b) C75 and (c) C110, while (d) shows the ballistic limit as a function of the cube compressive strength.

Table 4
Recht–Ipson constants (a and p) and ballistic limit velocities (v_{bl}) for 50 mm thick concrete slabs of different type based on experimental tests and numerical simulations.

Concrete Type	Experimental			Numerical			Difference in v_bl [%]
	a	p	v_{bl} [m/s]	a	p	v_{bl} [m/s]	
C35	0.99	1.35	119.7	0.91	1.69	117.7	1.7
C75	0.98	1.47	140.4	0.91	1.79	132.2	5.8
C110	1.00	1.33	152.6	0.92	1.61	141.8	7.1

1 defines a circle in the deviatoric stress space. In this study, the following expression for the normalised shape factor is adopted

$$e = \begin{cases} 0.65 & P^* < 0 \\ 0.65 + (1 - 0.65)\dfrac{P^*}{P^*_{\text{ref}}} & 0 \le P^* \le P^*_{\text{ref}} \\ 1.0 & P^* > P^*_{\text{ref}} \end{cases} \tag{13}$$

where P^*_{ref} is taken as 10.

The total damage effect in the MHJC model is calculated as

$$(1 - D) = \sqrt{(1 - D_S)(1 - D_C)} \tag{14}$$

where D is the total damage, D_S is the shear damage and D_C is the compaction damage. The evolutions of the shear and compaction damage are defined by

$$\dot{D}_S = \frac{\dot{\varepsilon}^p_{eq}}{\varepsilon^p_f}, \quad \dot{D}_C = \frac{\dot{\mu}^p}{\mu_{lock}} \tag{15}$$

while the plastic strain to fracture is found as

$$\varepsilon^p_f = a(P^* + T^*)^\beta \ge \left(\varepsilon^p_f\right)_{min} \tag{16}$$

where a and β are material constants, and $(\varepsilon^p_f)_{min}$ is introduced to provide a finite amount of plastic strain before fracture. Further, $\dot{\mu}^p$ is the plastic volumetric strain rate and μ_{lock} is the plastic volumetric strain of a fully compacted material. The volumetric strain μ is defined by $\mu = \frac{\rho}{\rho_0} - 1$ where ρ and ρ_0 are the current and initial mass densities, respectively.

The quasi-static, undamaged shear-pressure response of the MHJC model for three Lode angles and typical values for B, N, T^* and S_{max} is shown in Fig. 12(a), while the pressure-volume response is illustrated in Fig. 12(b). Note that the details in the derivation of the pressure-volume response is omitted here for brevity, and it is referred to [10] for a complete description of the MHJC model. It is implemented in LS-DYNA R12 [35] as a UMAT.

5.2. Model calibration

The MHJC model was calibrated based on the material tests in Section 3. The cylinder compressive strength f_c, the tensile strength f_t and the density ρ_0 were taken directly from the test results as given in Table 2. In addition, the reference strain rate $\dot{\varepsilon}_0$ was taken as the strain rate used in the material tests. From elasticity, the values $P_{crush} = f_c/3$ and $\mu_{crush} = f_c/(3K_1)$ were obtained, where K_1 is the initial bulk modulus. The Poisson ratio ν determined from the cube compression tests (see Table 2) was used to determine K_1 through the following relation

$$K_1 = \frac{2G(1 + \nu)}{3(1 - 2\nu)} \tag{17}$$

in which the shear modulus G was determined by inverse modelling as described below.

A 2D axisymmetric model of the cylindrical compression test was set up using the explicit non-linear finite element solver LS-DYNA R12 [35]. Thus, the engineering stress-strain curves from the cylinder compression tests in Fig. 5(a) were used as target curves for the optimization procedure. Note that the target curves only extend to the peak stress, so any post-peak behaviour is not included in the calibration. The model consisted of a rigid fixed bottom plate, the concrete cylinder, and a moving top plate which compressed the cylinder exactly as in the experiments. Contact between the parts was enforced by the penalty method (2D automatic surface-to-surface in LS-DYNA). Baltay and Gjelsvik [50] have reported values for the friction coefficient μ_{fric} between steel and concrete in the range 0.2 to 0.6. Both extremes of this range were simulated, and no notable difference was observed so a value of 0.4 was chosen. Friction is more influential for the cube compression test and is omitted altogether in the ballistic impact simulations as a conservative estimate [10].

The element size for the cylinder was chosen to be 1.0 mm, which makes the mesh 50 × 200 elements (radius × height). The mesh was regular and consisted of reduced integration 4-node volume weighted axisymmetric elements (element type 15 in LS-DYNA). The same element type was used for the rigid plates, with an element size of 4.5 mm. A sketch of the setup is shown in Fig. 13(a). A time scaling factor of 0.5×10^{-4} was applied, which means that the simulated time was 10-20 ms depending on the test. The velocity of the top plate was ramped up smoothly to a value of 1.5 mm/s to compress the cylinder. To avoid strain-rate effects in the material, the strain-rate sensitivity exponent C was set to zero for the calibration simulations. The kinetic energy in the simulation results was below 1 % in all cases and the energy ratio was between 0.99 and 1.0. This numerical model was then used to calibrate parts of the material model for all three concrete types.

The shear modulus G, the pressure hardening constants B and N, and the damage parameters α and β were all found by inverse modelling using an LS-OPT [51] procedure. Through several iterations the parameters were varied to minimise the difference (in a least squares sense) between the target curves (Fig. 5(a)) and the corresponding curves arising from the simulation. The yellow dots in Fig. 13(a) are 180 mm apart and indicate the position of the nodes used to estimate the axial compressive engineering strain from the numerical results exactly like in the material tests. The positions of measurements are the same as those used experimentally with DIC. The engineering stress was obtained by dividing the force through the specimen by its cross-sectional area. The resulting curves and their experimental counterparts are plotted in Fig. 14, and the material constants obtained are listed in Table 5. Note that the obtained parameters are not necessarily unique and that they may represent a local minimum. Ideally, one should have triaxial test data for a more accurate calibration of the shear strength versus pressure. In this case, where the slabs are thin and there is little to no tunnelling (see Fig. 8), this relationship should not dominate the response. For thicker slabs and deep penetration problems the shear strength versus pressure is assumed to be more significant.

5.3. Finite element model of ballistic impact tests

The 2D axisymmetric model of the ballistic impact tests was given the same element type and size (1.0 mm) as the material calibration simulations above using a computational cell approach [52]. This was done to minimize the mesh size dependency. Elements in a penetration analysis are prone to severe deformation and distortion and were thus set to erode when the equivalent strain exceeded a value of 1.0 or the time step of the element dropped below 1/1000th of its initial value. Note that this erosion scheme appeared to work better in R12 of LS-DYNA compared with prior releases. The penalty-based 2D automatic single surface contact option was used with zero friction as a conservative choice. The concrete slab was fixed at the boundary 260 mm from the centre but was otherwise free. Hourglass type 6 was chosen with default values to prevent zero-energy deformation modes. The MHJC model, implemented as a UMAT in LS-DYNA R12 as described in Section

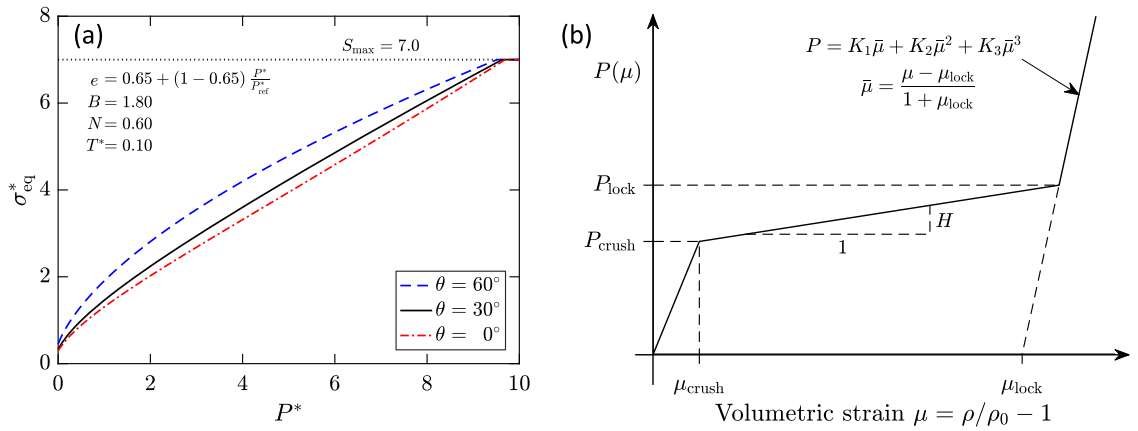

Fig. 12. (a) Shear-pressure strength relationship where $\theta = 0°$, $\theta = 30°$ and $\theta = 60°$ represent generalised tension, shear, and compression, respectively, and (b) pressure-volume response of the MHJC model where P_{crush}, P_{lock}, μ_{crush}, μ_{lock}, K_1, K_2 and K_3 are material constants defined in Section 5.2, and $H = (P_{lock} - P_{crush})/\mu_{lock}$.

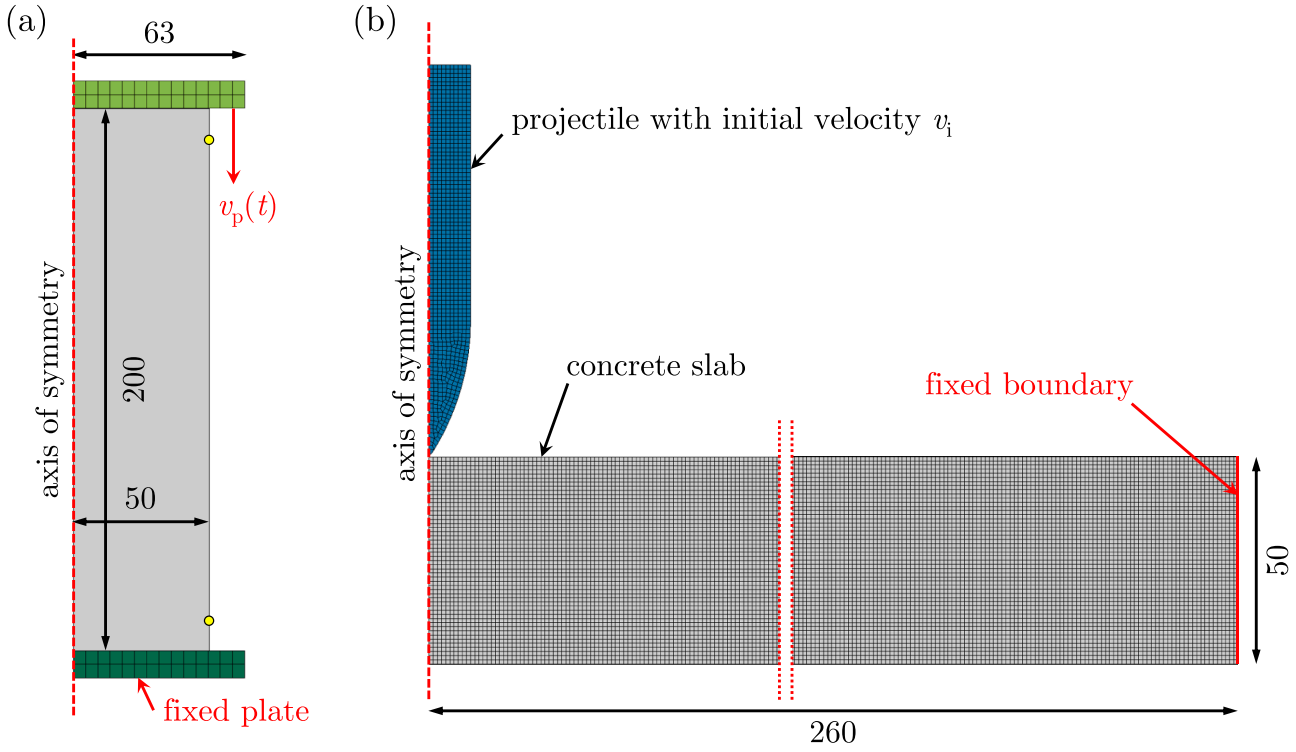

Fig. 13. Setup of 2D axisymmetric finite element simulations for (a) cylinder compression test and (b) ballistic impact tests.

5.1 and with material constants as given in Table 5, was used for the concrete types in all simulations. No data at elevated strain rates was available for the concretes used herein, so a value of C equal to 0.04 was chosen [10]. A sketch of the FE model can be seen in Fig. 13(b). Next, the projectile was modelled with an elastic-plastic model with linear isotropic hardening (*MAT_003 in LS-DYNA). Based on previous results [53], the projectile was assigned a Young's modulus of 204000 MPa, a Poisson ratio equal to 0.33, a yield stress of 1900 MPa and a tangent modulus equal to 15000 MPa. The specific mass was set to 7802 kg/m^3 to make the total mass of the projectile 196 g as in the tests. Initial velocities ranging from 125 m/s to 300 m/s were assigned to the projectile, and its velocity-time data was logged throughout the analyses. The simulated time was 2.0 ms in all analyses.

5.4. Numerical results

The run time for the analyses was approximately 10 minutes when run in parallel on 8 CPUs of a high-performance computing cluster. Results in terms of ballistic limit curves are shown and compared to the experimental data in Fig. 11 for all three concrete types. The relative differences between the concrete types were maintained in the simulation results, and the ballistic limit velocities were determined by a least squares fitting of a, p and v_{bl} in the Recht-Ipson model to the simulated residual velocities in a similar way as for the experimental tests. This resulted in ballistic limit velocities v_{bl} of 117.7 m/s, 132.2 m/s and 141.8 m/s for C35, C75 and C110, respectively (see also Table 4). The main finding of these results is an acceptable accuracy despite model simplifications. The qualitative results are also satisfying, as illustrated by Fig. 15 where the maximum volumetric strain is shown as fringe plots

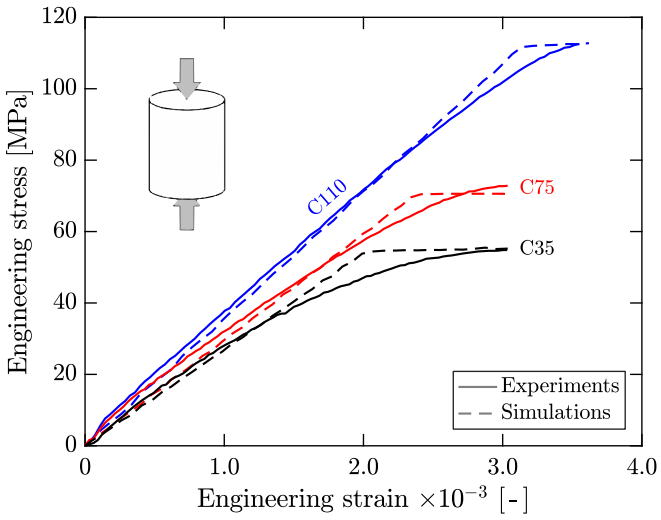

Fig. 14. Engineering stress-strain curves from tests and simulations of C35, C75 and C110 cylinders using the MHJC model with material constants from Table 5, where the solid lines are the experimental results from Fig. 5(a) and the dashed lines are the simulation results.

Table 5
Material constants used in the MHJC model.

Parameter	From	C35	C75	C110
ρ_0 [kg/m^3]	Tests	2467	2506	2570
f_c [MPa]	Tests	54.8	72.8	112.5
f_t [MPa]	Tests	4.0	5.2	6.2
$\dot{\varepsilon}_0$ [1/s]	Tests	10^{-5}	10^{-5}	10^{-5}
P_{crush} [MPa]	$f_c/3$	18.3	24.3	37.5
μ_{crush} [-]	$f_c/(3K_1)$	$2.15{\cdot}10^{-4}$	$2.85{\cdot}10^{-4}$	$4.41{\cdot}10^{-4}$
K_1 [MPa]	Eq. (17)	17291	18291	20468
G [MPa]	LS-OPT	10375	11505	14093
B [-]	LS-OPT	1.693	1.422	1.570
N [-]	LS-OPT	0.584	0.410	0.477
α [-]	LS-OPT	0.209	0.058	0.438
β [-]	LS-OPT	2.552	1.888	1.246
$(\varepsilon_f^p)_{min}$ [-]	Literature	0.002	0.002	0.002
K_2 [MPa]	Literature	-171000	-171000	-171000
K_3 [MPa]	Literature	208000	208000	208000
P_{lock} [MPa]	Literature	800	800	800
μ_{lock} [-]	Literature	0.01	0.01	0.01
C [-]	Literature	0.04	0.04	0.04

at various instants during the penetration process. The general shape of the strain pattern resembles the experiments, and the scabbing cone extends approximately to the centre of the slab although its diameter is underestimated and there is no fragmentation.

A parameter study applying the MHJC model on the two most quantifiable and accessible material parameters, namely f_c and f_t, was carried out on the C110 concrete. One parameter was altered at a time, either halved or doubled, to investigate its effect on the ballistic limit as determined by a least squares fit to the Recht-Ipson model as above. As such, the range of velocities from 125 m/s to 300 m/s was re-simulated with the new parameter values. Halving the unconfined compressive strength from 112.5 MPa to 56.25 MPa represents a change from a high-strength concrete to a normal strength concrete. This reduced the estimated ballistic limit by 9.4 %, which is a notable but not a significant change. However, doubling f_c to 225.0 MPa gave an increase in ballistic limit of only 4.6 %. This result suggests an asymptotic behaviour of the ballistic limit with respect to f_c for these slabs and this model, although modifying only f_c does not account for other properties that are usually correlated with f_c, for instance the stiffness. On the other hand, changing the tensile strength f_t had a much larger effect on the ballistic limit. Halving f_t reduced v_{bl} by 23.0 % while doubling f_t gave a 22.8 % increase. This indicates that v_{bl} depends strongly on f_t for thin concrete slabs.

Another important effect is the strain-rate sensitivity. There is no data on strain-rate effects for the specific concretes used herein, and the effect can be difficult to quantify experimentally. Based on the literature [10,18], the parameter C was chosen equal to 0.04 in the baseline model. Another series of simulations with $C = 0$ and $C = 0.08$ were run to highlight its effect on the ballistic limit. Removing strain-rate effects entirely lowered v_{bl} by 20.7 %, while increasing C to 0.08 increased the ballistic limit by only 4.4 %. With the results of the baseline model already on the conservative side, it appears both safe and reasonable to include strain-rate effects. Friction is another parameter that is difficult to quantify, and it was thus conservatively assumed to be zero. Including friction with $\mu_{fric} = 0.4$ (assumed equal for static and dynamic friction) naturally decreased the projectile's residual velocity somewhat, thereby increasing v_{bl} by 5.1 %. The projectile nose must push material out of the way to make room for penetration and perforation. The sliding of material along the nose dissipates energy when $\mu_{fric} > 0$, and this process is more pronounced in the simulations compared with the experiments where there is extensive fragmentation. Finally, the effect of the mass density ρ_0 was also investigated. Doubling and halving ρ_0 increased and decreased the ballistic limit by 3.6 % and 4.7 %, respectively. These results align with previously obtained experimental data [11], where the ballistic limit of 100 mm thick concrete slabs increased from 283 m/s to 299 m/s when increasing the density from 2520 kg/m^3 to 3828 kg/m^3 by adding high density fine aggregate. The results of the parameter studies are summarised in Fig. 16, while Fig. 17 shows how the ballistic limit curves for C110 are altered when f_c and f_t are varied.

Finally, velocity-time curves of the projectile from the simulations and the experiments (based on the subset tracking algorithm available in eCorr [40] – see Section 4.2) are compared in Fig. 18 for slabs (a) C35-11, (b) C75-12 and (c) C110-5. It is noted that the qualitative shape of the numerically obtained curves resemble the experimental ones. Firstly, the projectile starts to decelerate while continuing to penetrate the slab. This phase is similar in the tests and in the simulations. When the nose emerges at the rear side of the target, the velocity-time curve gradually changes to a horizontal line, which is the residual velocity. Once the projectile nose has passed the rear surface of the slab, it exits unimpeded in the simulations. In the experiments, however, fragments due to scabbing from the back side of the concrete slabs are present which may slow the projectile down. When the end of the projectile is no longer visible in the high-speed camera video from the front side, the curve is dashed until the projectile again is visible on the back side of the slab. A linear dotted line is drawn for visualization and to bridge this gap like in Fig. 10, but this path is likely non-linear. It is during this section that the fragments may cause the projectile to decelerate in the experiment.

6. Discussion

While the compressive strength of the concrete is important in many respects, the tensile strength seems to be a more significant parameter for discussing the perforation resistance of thin concrete slabs [54]. The relation suggested in Fig. 11(d) may therefore be better described in terms of the tensile strength than the compressive strength. The tensile strength of each concrete type was estimated from tensile splitting tests. These tests possibly underestimate the tensile strength of the material [55], which results in conservative estimates of f_t. A consequence of this underestimation is the underprediction of the ballistic limit velocity by the FE simulations, since f_t was taken directly from the tensile splitting tests. From the C35 to the C110 concrete, the unconfined compressive strength increases by 260 % while the tensile strength only increases by 55 % (Table 2), and finally the ballistic limit velocity increases by

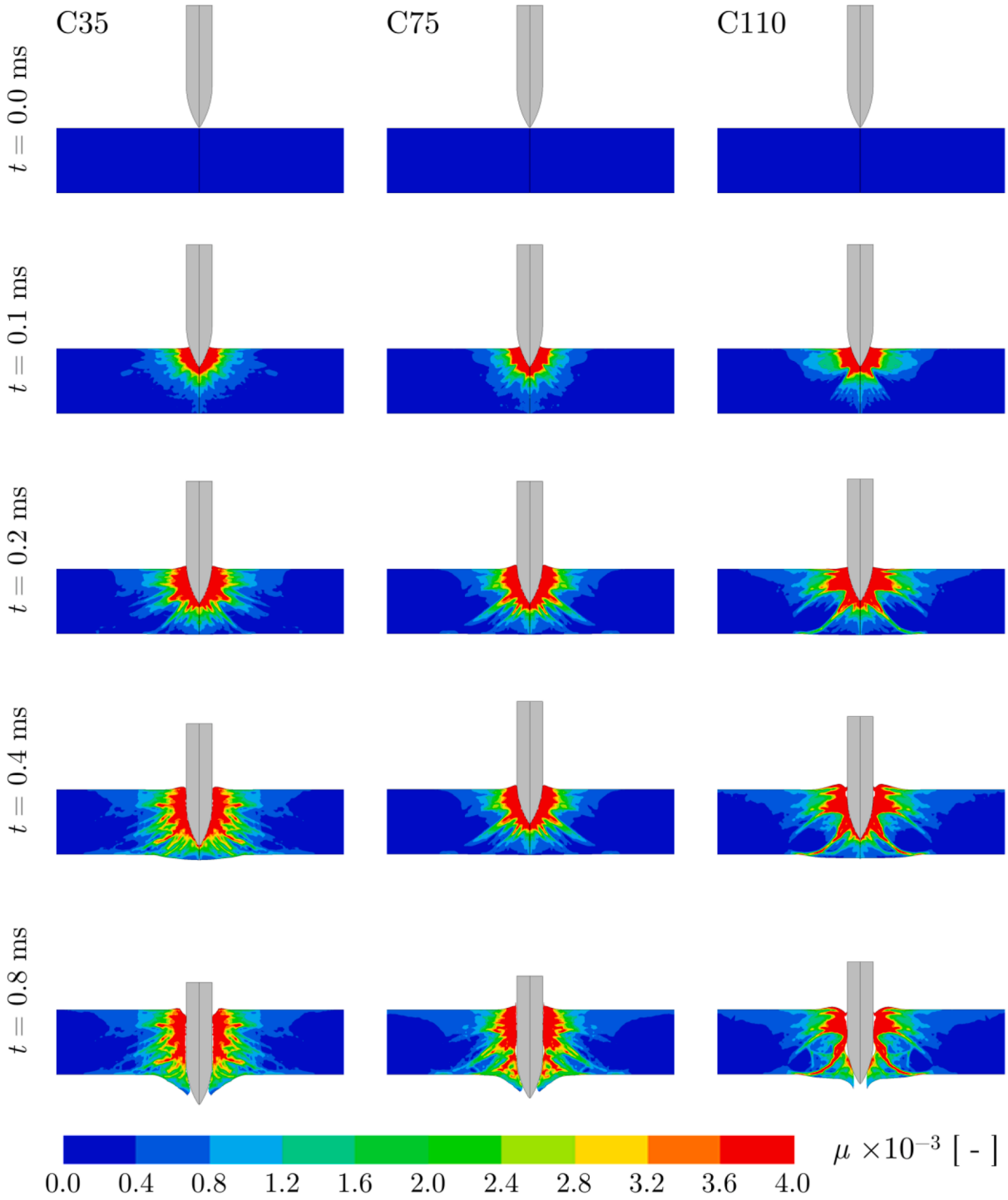

Fig. 15. Fringe plot of the maximum volumetric strain at selected times from finite element simulations of the perforation of C35 concrete (left column), C75 concrete (centre column) and C110 concrete (right column) where the initial velocity of the projectile was 150 m/s.

approximately 27 % (Table 4). It is established that it is difficult to increase the tensile strength proportionally to the compressive strength for concretes with unconfined compressive strengths above 75 MPa [56]. Also, one cannot expect an increase in ballistic limit directly in line with the increase in tensile strength because other parameters such as inertia, strain-rate sensitivity, friction, etc., all influence the results, although less than f_t. Using a coefficient of friction equal to 0.4 in the ballistic simulations increased v_{bl} by a modest 5.1 % for the C110 concrete, which is attributed to the sustained contact between the projectile nose and the slab during perforation. With no excessive fragmentation in the FE results, the projectile nose must displace the material to perforate the slab. In the experiments, the spalling and scabbing cones meet in the centre of the slab, leaving only a small portion of the hole with a diameter close to the projectile diameter. Thus, the effect of friction might be overestimated in the simulations.

The shear modulus G, the pressure hardening constants B and N, and the damage parameters α and β were all found by inverse modelling using a LS-OPT procedure on an axisymmetric model of the cylinder

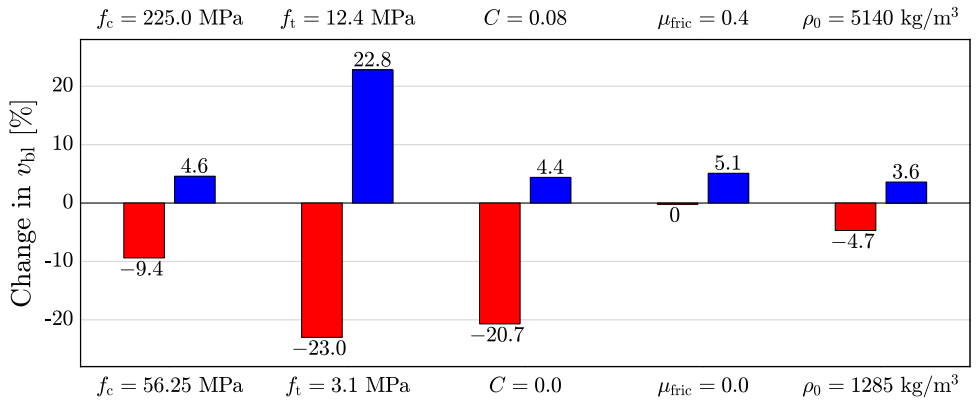

Fig. 16. Results from the parameter studies for C110 applying the MHJC model.

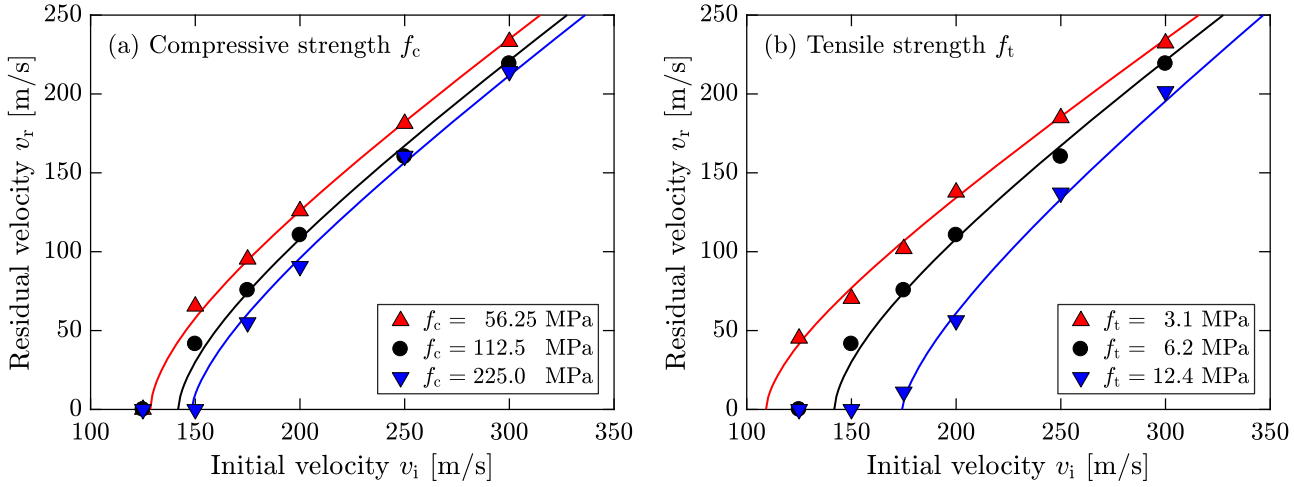

Fig. 17. Comparison between numerically obtained ballistic limit curves for C110 when (a) changing f_c, and (b) changing f_t.

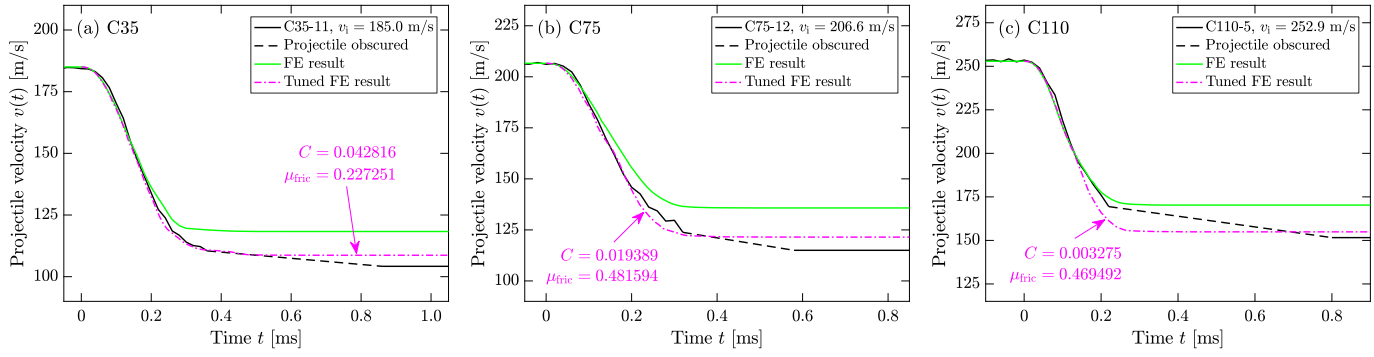

Fig. 18. Experimental and numerical velocity-time profiles for slab (a) C35-11, (b) C75-12 and (c) C110-5.

compression tests. The experimental engineering stress-strain curves estimated by DIC were used as target curves in the numerical optimisation for the calibration of each concrete type. The parameters f_c, f_t, ρ_0, $\dot{\varepsilon}_0$ and ν were established from the material tests, and the remainder was taken from the literature or found through analytical relations. This procedure resulted in a good numerical representation of the cylinder compression tests, which Fig. 14 confirms. The post-peak behaviour was not included in the calibration, partly because the deformation became very inhomogeneous and the strain measurements deviated significantly depending on where it was measured. The behaviour of the concretes at this stage could, however, be important in the perforation simulations. Triaxial compression tests are also warranted if a proper calibration of the pressure hardening is needed [57]. Cube compression tests may provide better data for the pressure hardening because of the confinement and friction, but this requires full 3D analyses which is beyond the scope of this study. The low thickness of the slabs in this study resulted in little confinement and pressure hardening, rendering this data less important, and the absence of a tunnelling section as shown in Fig. 8 supports this assertion. The tunnelling region between the spalling and scabbing cones is the area where the highest levels of confinement are typically found.

While strain-rate effects in concrete seem to initiate at lower rate values for tension than for compression [42,58], the constitutive relation used herein is symmetric with respect to strain-rate sensitivity in

compression and tension. Further, the model is primarily developed for penetration problems in concrete where a high level of pressure is expected [18]. As mentioned, there is little confining pressure in this case and thus tensile stresses dominate the problem as Fig. 16 attests to.

Table 4 compares ballistic limit velocities and Recht-Ipson constants between experimental tests and numerical simulations. As seen, the agreement in ballistic limit velocity is in general good, especially for the C35 concrete. However, the slope of the f_{cc} - v_{bl} curve shown in Fig. 11 (d) differs between tests and simulations. Experimentally the ballistic limit velocity increased by 27 % going from the C35 to the C110 concrete, while the corresponding numerical increase was 20 %. A possible reason for this could be that the DIC instrumented tests which produced the engineering stress-strain curves used in the calibration for the C35 concrete were carried out 41 days after casting, whereas the ballistic impact tests were performed at $D_t = 33$ days. For the C75 concrete these values were 28 and 29 days, respectively, while for the C110 concrete the material tests with DIC were conducted 28 days after casting and the impact tests 43 days after casting (see Fig. 2). This shift could cause an overestimation of the strength of the C35 concrete and an underestimation of the C110 concrete in the simulations, thereby causing the differing slopes in the f_{cc} - v_{bl} curve shown in Fig. 11(d). In addition, the curing conditions for the slabs were not identical to the curing conditions for the material test specimens. Table 3 also reveals that the average target thickness was in general 2-3 % higher than the nominal value, while all the numerical simulations were run using the nominal thickness of 50 mm. Increasing the target thickness by 2-3 % would increase the numerical ballistic limits slightly and bring them closer to the experimental values (see also Table 4). Note finally that the numerical model assumes that the strain rate sensitivity is the same for all concrete types, which is probably unprecise.

Further, in the Recht-Ipson model the constant a determines the slope of the v_i - v_r curve, while p describes the "jump" of this curve at the ballistic limit velocity. The jump in residual velocity at the ballistic limit has been found to increase with target thickness and impact velocity, at least in metallic materials [59]. Both tests and simulations in this study gave values of a close to unity (between 0.9 and 1), while the values of p differed more (around 1.4 experimentally and 1.7 numerically). The effect of this difference is visible in Fig. 11, showing that the jump in residual velocity at the ballistic limit is stronger numerically than experimentally. A plausible explanation for this behaviour is that concrete pieces due to scabbing affects the perforation process more in the experiments than in the simulations, preventing the projectile to slide freely through the target after punching a hole. Support for this conjecture can be seen in the velocity-time plots in Fig. 18, showing that the residual velocity of the projectile becomes constant faster in the numerical simulations than in the experiments. In the simulations, the elements are simply eroded at fracture, thereby losing their resistance.

The FE analyses had fast run times and gave good and conservative results. This model can therefore be considered useful for engineering assessments during the design phase of concrete protective structures. Using the same element size in the material test and the component test simulations in a computational cell approach is an accepted way to reduce mesh-size dependency [52]. The FE model and constitutive relation used in this study are not overly complicated and increasing the sophistication in either is expected to improve the accuracy of the results. Extending from 2D axisymmetric to full 3D would allow for the inclusion of pitch and possible rotation of the projectile during penetration, in addition to rebars, but at the cost of a significant increase in the computational time. Using smoothed particle hydrodynamics (SPH) instead of finite elements could be an alternative approach to describe spalling, scabbing, and fragmentation [60].

By tuning unfixed parameters such as the strain-rate sensitivity constant C and the friction coefficient μ_{fric}, alignment of the FE results with the experimental data is achievable. This is exemplified in Fig. 18, but those results are inconsequential. The resulting parameters are not internally consistent and by no means unique – other values can provide just as good results. Hence, tuning the parameters in this sense provides little or no new insight other than showing that it is possible to improve the results if these values were known. The aim of the simulations was to investigate how well the MHJC constitutive relation and a 2D axisymmetric FE model could predict the ballistic perforation resistance of concrete slabs impacted by ogive-nose steel projectiles using standard material tests and two-dimensional digital image correlation to calibrate the constitutive relation. The MHJC model was demonstrated to give good predictions on the conservative side of the experimentally obtained ballistic limit curves.

Conclusions

Based on the experimental work performed the following conclusions are drawn:

- The three commercially produced concrete types had the expected compressive strength relative to each other, and the compressive test results always showed higher values than the nominal values specified when ordering the concrete.
- All three concrete types still had significant strength development after 28 days, so it is generally advisable to carry out both the material tests and the component tests within a short period of time.
- The ballistic limit of the slabs increased almost linearly with concrete strength. For the thin slabs, the tensile strength appears to be the most dominant material parameter.
- The scabbing diameter was always larger than the spalling diameter, and both diameters seemed to increase with increasing concrete strength. There was hardly any tunnelling section between the scabbing and spalling areas due to the low thickness of the slabs.
- Digital image correlation was found to successfully estimate stress-strain curves for the materials and for measuring the projectile velocities before, during and after impact.

The axisymmetric FE simulations had a low computational cost and gave accurate results. Thus, using axisymmetric models instead of full 3D models for ballistic impact can be a useful approach in the design phase of a protective concrete structure. The main findings from the FE analyses can be listed as follows:

- As laid out in Table 4, material parameters for the MHJC model were obtained from three different sources: i) directly from material tests and through analytical relations, ii) from inverse modelling, and iii) from the literature. The resulting sets of parameters were able to accurately reproduce the cylinder compression tests in terms of engineering stress-strain curves for all concrete types.
- Using the calibrated models and making reasonable assumptions produced good, conservative numerical predictions of the ballistic limit velocities of the slabs.
- Like the experiments, the numerical simulations indicated that the tensile strength exerts a significant influence on the ballistic impact properties of these thin slabs.
- Parameter studies using the MHJC model show that it is important to include strain-rate effects in the constitutive relation, and that friction may be an influential unknown in numerical models. Friction can also be difficult to measure experimentally.
- The MHJC model is easy to calibrate and implement, and it provides a good and reliable alternative to more advanced concrete models for which accurate material parameter sets may be difficult to obtain.

CRediT authorship contribution statement

Martin Kristoffersen: Conceptualization, Methodology, Formal analysis, Visualization, Software, Investigation, Writing – original draft, Writing – review & editing. **Oda L. Toreskås:** Conceptualization, Investigation, Writing – original draft, Funding acquisition. **Sumita**

Dey: Conceptualization, Investigation, Writing – original draft, Writing – review & editing, Funding acquisition. **Tore Børvik:** Conceptualization, Methodology, Investigation, Writing – original draft, Writing – review & editing, Project administration, Funding acquisition.

Declaration of Competing Interest

The authors declare that they have no known competing financial interests or personal relationships that could have appeared to influence the work reported in this paper.

Acknowledgment

The present work has been carried out with financial support from the Norwegian Defence Estates Agency and the Centre of Advanced Structural Analysis (CASA), Centre for Research-based Innovation, at the Norwegian University of Science and Technology (NTNU) and the Research Council of Norway through project no. 237885 (CASA). The authors would also like to acknowledge Mr. Steinar Seehuus, Mr. Trond Auestad, Ms. Guri Lillehaug and Ms. Marte Vestermo Nesje for assistance with the various experimental programmes.

References

[1] Corbett GG, Reid SR, Johnson W. Impact loading of plates and shells by free-flying projectiles: a review. Int J Impact Eng 1996;18:141–230.
[2] Luk VK, Forrestal MJ. Penetration into semi-infinite reinforced-concrete targets with spherical and ogival nosed projectiles. Int J Impact Eng 1987;6:291–300.
[3] Frew DJ, Hanchak SJ, Green ML, Forrestal MJ. Penetration of concrete targets with ogive-nose steel rods. Int J Impact Eng 1998;21:489–97.
[4] Hanchak SJ, Forrestal MJ, Young ER, Ehrgott JQ. Perforation of concrete slabs with 48 MPa and 140 MPa unconfined compressive strengths. Int J Impact Eng 1992;12:1–7.
[5] Dancygier AN, Yankelevsky DZ. High strength concrete response to hard projectile impact. Int J Impact Eng 1996;18:583–99.
[6] Kennedy RP. A review of procedures for the analysis and design of concrete structures to resist missile impact effects. Nucl Eng Des 1976;37:183–203.
[7] Adeli H, Amin M. Local effects of impactors on concrete structures. Nucl Eng Des 1985;88:301–17.
[8] Yankelevsky DZ. Local response of concrete slabs to low velocity missile impact. Int J Impact Eng 1997;19:331–43.
[9] Qian L, Yang Y, Liu T. A semi-analytical model for truncated-ogive-nose projectiles penetration into semi-infinite concrete targets. Int J Impact Eng 2000;24:947–55.
[10] Polanco-Loria M, Hopperstad OS, Børvik T, Berstad T. Numerical predictions of ballistic limits for concrete slabs using a modified version of the HJC concrete model. Int J Impact Eng 2008;35:290–303.
[11] Børvik T, Gjørv OE, Langseth M. Ballistic perforation resistance of high-strength concrete slabs. Concr Int 2007;29:45–50.
[12] Dancygier AN. Rear face damage of normal and high-strength concrete elements caused by hard projectile impact. ACI Struct J 1998;95:291–304.
[13] Dancygier AN. Effect of reinforcement ratio on the resistance of reinforced concrete to hard projectile impact. Nucl Eng Des 1997;172:233–45.
[14] Sliter GE. Assessment of empirical concrete impact formulas. J Struct Division 1980;106:1023–45.
[15] Lee S, Kim C, Yu Y, Cho JY. Effect of reinforcing steel on the impact resistance of reinforced concrete panel subjected to hard-projectile impact. Int J Impact Eng 2021;148:103762.
[16] Almansa EM, Cánovas MF. Behaviour of normal and steel fiber-reinforced concrete under impact of small projectiles. Cem Concr Res 1999;29:1807–14.
[17] Zhang X, Wu H, Zhang S, Huang F. Projectile penetration of reinforced concrete considering the effect of steel reinforcement: Experimental study and theoretical analysis. Int J Impact Eng 2020;144:103653.
[18] Holmquist TJ, Johnson GR, Cook WH. A computational constitutive model for concrete subjected to large strains, high strain rates and high pressures. In: Proceedings of 14th International Symposium on Ballistics. Quebec, Canadn; 1993.
[19] Riedel W, Thoma K, Hiermaier S, Schmolinske E. Penetration of reinforced concrete by BETA-B-500 numerical analysis using a new macroscopic concrete model for hydrocodes. In: Proceedings of the 9th International Symposium on the Effects of Munitions with Structures. Berlin-Strausberg, Germany; 1999. p. 315–22.
[20] Ågårdh L, Laine L. 3D FE-simulation of high-velocity fragment perforation of reinforced concrete slabs. Int J Impact Eng 1999;22:911–22.
[21] Kong X, Fang Q, Li QM, Wu H, Crawford JE. Modified K&C model for cratering and scabbing of concrete slabs under projectile impact. Int J Impact Eng 2017;108:217–28.
[22] Rajput A, Iqbal MA, Gupta NK. Ballistic performances of concrete targets subjected to long projectile impact. Thin-Walled Struct 2018;126:171–81.
[23] Liu J, Wu C, Su Y, Li J, Shao R, Chen G, Liu Z. Experimental and numerical studies of ultra-high performance concrete targets against high-velocity projectile impacts. Eng Struct 2018;173:166–79.
[24] Chen X, Lu F, Zhang D. Penetration trajectory of concrete targets by ogived steel projectiles–Experiments and simulations. Int J Impact Eng 2018;120:202–13.
[25] Xu LY, Xu H, Wen HM. On the penetration and perforation of concrete targets struck transversely by ogival-nosed projectiles – a numerical study. Int J Impact Eng 2019;125:39–55.
[26] Abdel-Kader M. Modified settings of concrete parameters in RHT model for predicting the response of concrete panels to impact. Int J Impact Eng 2019;132:103312.
[27] Cao YYY, Yu L, Tang WH, Brouwers HJH. Numerical investigation on ballistic performance of coarse-aggregated layered UHPFRC. Constr Build Mater 2020;250:118867.
[28] Sun S, Lu H, Yue S, Geng H, Jiang Z. The composite damage effects of explosion after penetration in plain concrete targets. Int J Impact Eng 2021;153:103862.
[29] Malvar LJ, Crawford JE, Wesewich JW, Simons D. A plasticity concrete material model for DYNA3D. Int J Impact Eng 1997;19:847–73.
[30] Kristoffersen M, Pettersen JE, Aune V, Børvik T. Experimental and numerical study on blast loading of normal strength concrete slabs. Eng Struct 2018;174:242–55.
[31] Riedel W, Kawai N, Kondo KI. Numerical assessment for impact strength measurements in concrete materials. Int J Impact Eng 2009;36:283–93.
[32] Grunwald C, Schaufelberger B, Stolz A, Riedel W, Borrvall T. A general concrete model in hydrocodes: Verification and validation of the Riedel–Hiermaier–Thoma model in LS-DYNA. Int J Prot Struct 2017;8:58–85.
[33] Lubliner J, Oliver J, Oller S, Oñate E. A plastic-damage model for concrete. Int J Solids Struct 1989;25:299–326.
[34] Kristoffersen M, Minoretti A, Børvik T. On the internal blast loading of submerged floating tunnels in concrete with circular and rectangular cross-sections. Eng Fail Anal 2019;103:462–80.
[35] Livermore Software Technology (LST), An Ansys Company. LS-Dyna Keyword User's Manual, LS-DYNA R12, 2020.
[36] ABAQUS. Analysis user's manual version 2019. SIMULIA; 2018.
[37] Chen WF. Plasticity in reinforced concrete. New York: Mc Graw Hill; 1982.
[38] Xu M, Wille K. Calibration of K&C concrete model for UHPC in LS-DYNA. Adv Mater Res 2014;1081:254–9.
[39] Xu X, Ma T, Ning J. Failure mechanism of reinforced concrete subjected to projectile impact loading. Eng Fail Anal 2019;96:468–83.
[40] https://www.ntnu.edu/kt/ecorr [accessed: 2021-05-27].
[41] Arıoglu N, Girgin ZC, Arıoglu E. Evaluation of ratio between splitting tensile strength and compressive strength for concretes up to 120 MPa and its application in strength criterion. ACI Mater J 2006;103:18–24.
[42] Lu YB, Li QM. About the dynamic uniaxial tensile strength of concrete-like materials. Int J Impact Eng 2011;38:171–80.
[43] Kristoffersen M, Hauge KO, Minoretti A, Børvik T. Experimental and numerical studies of tubular concrete structures subjected to blast loading. Eng Struct 2021;233:111543.
[44] Børvik T, Langseth M, Hopperstad OS, Malo KA. Ballistic penetration of steel plates. Int J Impact Eng 1999;22:855–86.
[45] Børvik T, Clausen AH, Hopperstad OS, Langseth M. Perforation of AA5083-H116 aluminium plates with conical-nose steel projectiles – experimental study. Int J Impact Eng 2004;30:367–84.
[46] Børvik T, Dey S, Clausen AH. Perforation resistance of five different high-strength steel plates subjected to small-arms projectiles. Int J Impact Eng 2009;36:948–64.
[47] Goldsmith W, Tam E, Tomer D. Yawing impact on thin plates by blunt projectiles. Int J Impact Eng 1995;16:479–98.
[48] Jinzhu L, Zhongjie L, Hongsong Z, Fenglei H. Perforation experiments of concrete targets with residual velocity measurements. Int J Impact Eng 2013;57:1–6.
[49] Recht RF, Ipson TW. Ballistic perforation dynamics. J Appl Mech 1963;30:384–90.
[50] Baltay P, Gjelsvik A. Coefficient of friction for steel on concrete at high normal stress. J Mater Civ Eng 1990;2:46–9.
[51] LS-OPT. LS-OPT support site. 2018. http://lsoptsupport.com [accessed: 2021-05-27].
[52] Ruggieri C, Panontin TL, Dodds RH. Numerical modeling of ductile crack growth in 3-D using computational cell elements. Int J Fract 1996;82:67–95.
[53] Børvik T, Hopperstad OS, Berstad T, Langseth M. A computational model of viscoplasticity and ductile damage for impact and penetration. Eur J Mech A/Solids 2001;20:685–712.
[54] Riera JD. Penetration, scabbing and perforation of concrete structures hit by solid missiles. Nucl Eng Des 1989;115:121–31.
[55] Resan SF, Chassib SM, Zemam SK, Madhi MJ. New approach of concrete tensile strength test. Case Stud Constr Mater 2020;12:e00347.
[56] FIB/CEB. State of the art report: high strength concrete. Switzerland; 1990.
[57] Antoniou A, Daudeville L, Marin P, Omar A, Potapov S. Discrete element modelling of concrete structures under hard impact by ogive-node steel projectiles. Eur Phys J Spec Top 2018;227:143–54.
[58] Pajak M. The influence of the strain rate on the strength of concrete taking into account the experimental techniques. Archit Civ Eng Environ 2011;3:77–86.
[59] Børvik T, Hopperstad OS, Langseth M, Malo KA. Effect of target thickness in blunt projectile penetration of Weldox 460 E steel plates. Int J Impact Eng 2003;28:413–64.
[60] Zhang S, Kong X, Fang Q, Chen L, Wang Y. Numerical prediction of dynamic failure in concrete targets subjected to projectile impact by a modified Kong-Fang material model. Int J Impact Eng 2020;144:103633.